Article

Combination of Scanning Strategies and Optimization Experiments for Laser Beam Powder Bed Fusion of Ti-6Al-4V Titanium Alloys

Wentian Shi [ID], Jihang Li, Yanlong Jing *, Yude Liu, Yuxiang Lin and Yufan Han

School of Artificial Intelligence, Beijing Technology and Business University, Beijing 100048, China; shiwt@th.btbu.edu.cn (W.S.); 2030602087@st.btbu.edu.cn (J.L.); liuyd@th.btbu.edu.cn (Y.L.); 2130062098@st.btbu.edu.cn (Y.L.); 1930301023@st.btbu.edu.cn (Y.H.)
* Correspondence: jingyanlong@btbu.edu.cn

Abstract: This paper studies the effects of different combinations of scanning strategies between layers on the surface quality, tensile properties, and microstructure of samples in a laser beam powder bed fusion (L-PBF) formation experiment of Ti-6Al-4V titanium alloy. The purpose of this experiment was to improve the comprehensive performance of the piece by selecting the optimal combination of scanning strategies. The results show that the surface roughness of the L-PBF specimen was the lowest under the combination of the CHESS scanning strategy, reaching 14 μm. The surface hardness of the samples was generally higher with the LINE scanning strategy and the angle offset of 90°, reaching 409 HV. The overall density of the samples was higher under the combination of CHESS scanning strategies, reaching 99.88%. Among them, the CHESS&45° sample had the best comprehensive properties, with a density of 99.85%, a tensile strength of up to 1125 MPa, a yield strength of 912 MPa, and an elongation of 8.2%. The fractured form was a ductile fracture, with many dimple structures. Compared with the CHESS scanning strategy, the tensile properties of the CHESS&45° samples were improved by 12.8%. The microstructure of the L-PBF sample was mainly composed of the primary β phase and α′ martensite phase. The upper surface of the CHESS scanning strategy combination sample had a clear melt channel, and the distribution of each phase was uniform. A certain number of columnar β crystals were distributed in the longitudinal section of the sample, which was paralleled to the build direction. The columnar β crystals of CHESS&45° were relatively coarse, which enhanced the tensile properties of the sample.

Keywords: laser beam powder bed fusion; TC4; scanning strategy; surface quality; mechanical properties

1. Introduction

Laser beam powder bed fusion (L-PBF) is one of the most widely used and researched metal additive manufacturing (AM) technologies and belongs to the powder bed melting technology, which is based on the principle of using a high-energy laser beam to melt a metal powder bed layer by layer to create solid parts [1–9]. L-PBF technology is widely used in automobile manufacturing [10], aerospace [11,12], and medical industries [13,14]. L-PBF technology is more widely used in the medical field, including orthopedic implants, dental implants [14], etc. At the same time, the forming materials of L-PBF technology include iron-based [15], titanium-based [14], and nickel-based materials [16]. Since the properties of L-PBF-formed Ti-6Al-4V (TC4) titanium alloys vary with their microstructures and have directional anisotropy [17], different scanning strategies have essential effects on the microstructure of the L-PBF samples [18,19]. At the same time, the scanning strategy has a particular influence on the anisotropy of the formation, and the anisotropy of the forming sample is closely related to the resistivity and other properties of the material [20]. Amir Mahyar Khorasani et al. [21] investigated the single-contour-and-fill method (SC+F)

to form lattice structures and find the potential of the unfilled single-contour (SC) scanning strategy to improve the reproducibility of porous lattices. Meanwhile, SC proved to be a feasible strategy to produce Ti-6Al-4V lattices with pillar diameters below 350 μm. Peng Wang et al. [22] analyzed the effects of process parameters on the build surface, relative density, defects, microstructure, and mechanical properties of parts through multilayer fabrication and surface optimization experiments. The study found that the dot pitch had the most significant impact on the build surface of the manufactured part, and when the dot pitch was 35 μm, unmelted defects could be eliminated. Zhenyu Yan et al. [23] found that the anisotropy of the mechanical properties of the L-PBF samples increased significantly with the residence time between the forming layers. Weihong Cen et al. [24] proposed a triangular wave strip scanning strategy. This scanning strategy not only improves the quality of the lap area but also increases the tensile strength and Vickers hardness of the sample, and the density of the 316 L stainless steel sample reaches 99.74%. Sheng Zou et al. [25] found that under the multi-laser L-PBF process, careful scan order and direction planning to reduce heat concentration was beneficial for controlling residual stress. Wenhui Yu et al. [26] adopted two remelting processes with the same initial scanning strategy and opposite directions in the formed AlSi10Mg parts using L-PBF technology. They found that the porosity in the central region of the samples with the two remelting processes was almost at the same level. However, there were differences in the porosity distribution at the front of the melt channel and in the wake of the co-remelting strategy. Xiaofeng Li et al. [27] studied the effect of different structural angles on the microstructure and mechanical properties of AlSi10Mg alloys. The surface hardness of the sample at 45° was the highest, reaching 154.44 HV. The 60° specimen had good mechanical properties, with a tensile strength of 463.54 MPa, a yield strength of 283.37 MPa, and an elongation of 9.25%. R. Rashid et al. [28] found that the relative density of the samples printed using the dual-scan strategy increased compared to the samples printed using the single scan strategy. Furthermore, it was observed that the samples fabricated using the dual-scan strategy showed higher stiffness than those printed using the single scan strategy. R. Rashid et al. [29] obtained a yield strength between 225 MPa and 263 MPa, a tensile strength between 260 MPa and 365 MPa, and a ductility between 1 and 4%, when the tensile samples were printed with AlSi12 aluminum alloy in three different orientations, horizontal (H—0°), inclined (I—45°), and vertical (V—90°). Ryan Cottam et al. [30] found that there was significant variation in the dislocation densities between the SLMed and the EBMed samples, although a similar manufacturing techniques were used. Most of the above studies focus on zoned scanning and changing the scanning offset angle to make the sample have better properties in a specific direction. Nevertheless, there are few studies on the change in the scanning strategy between the forming layers. In this paper, the combined method of LINE scanning, CHESS scanning, and STRIPE scanning strategies combined with a directional angle offset scanning strategy was studied to explore the surface quality, mechanical properties, and microstructure of L-PBF samples under different processing methods. The purpose of this experiment was to find the optimal process combination to directionally enhance the mechanical properties of the specimen while having better surface quality.

2. Materials and Methods

2.1. L-PBF Forming Materials and Equipment

The experiment material was TC4 titanium alloy powder (FeiErkang Rapid Manufacturing Technology Co., Ltd., Wuxi City, Jiangsu Province, China; prepared using gas atomization method), and the size was 15–53 μm (D10:19.46; D50:38.96; D90:61.52). Figure 1 and Table 1 show the powder particle morphology and component content, respectively. In this experiment, a metal 3D printer (AM400; Renishaw plc, London, UK) was used as the L-PBF forming device with a maximum power of 400 W and a laser wavelength of 1075 nm. The laser beam diameter of this equipment is 70 μm, and the maximum size of the formed part is 250 mm × 250 mm × 300 mm.
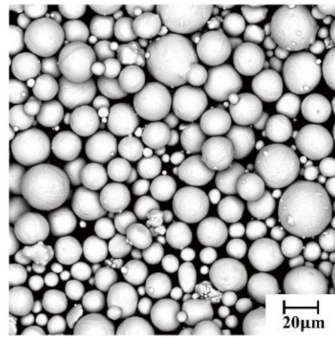
Figure 1. SEM morphology of TC4 titanium alloy powder particles.

Table 1. Chemical composition of TC4 titanium alloy powder.

Element	Ti	Al	V	Fe	C	N	H	O
Wt.%	Balance	5.5~6.5	3.5~4.5	0.25	0.08	0.03	0.0125	0.13

2.2. L-PBF Forming Parameters and Scanning Strategy Combination Design

Based on the previous basic pre-test and combined with the research of Saurabh Kumar Gupta [31] et al., the selection of L-PBF forming parameters was shown in Table 2. The formula for calculating the scanning speed is the point distance (μm) divided by the exposure time (μs). The scanning speed in this experiment is 500 mm/s.

Table 2. L-PBF forming parameters.

Parameter	Value
Laser power (W)	250
Exposure time (μs)	100
Point distance (μm)	50
Hatch space (mm)	0.07
Scanning speed (mm/s)	500
Layer thickness (μm)	50

A combination of common scanning strategies and directional angle offset scanning strategies was selected in this experiment. The commonly used scanning strategies included LINE scanning, CHESS scanning, and STRIPE scanning. The directional angle offset scanning strategies were divided into 0°, 45°, and 90° relative to the tensile direction of the sample. The common scanning strategy was that each layer was deflected by 67°. The combination of different scanning strategies and the size of the tensile specimen is shown in Figure 2 and Table 3.

Table 3. Different L-PBF tensile specimen numbers and their scanning strategy combinations.

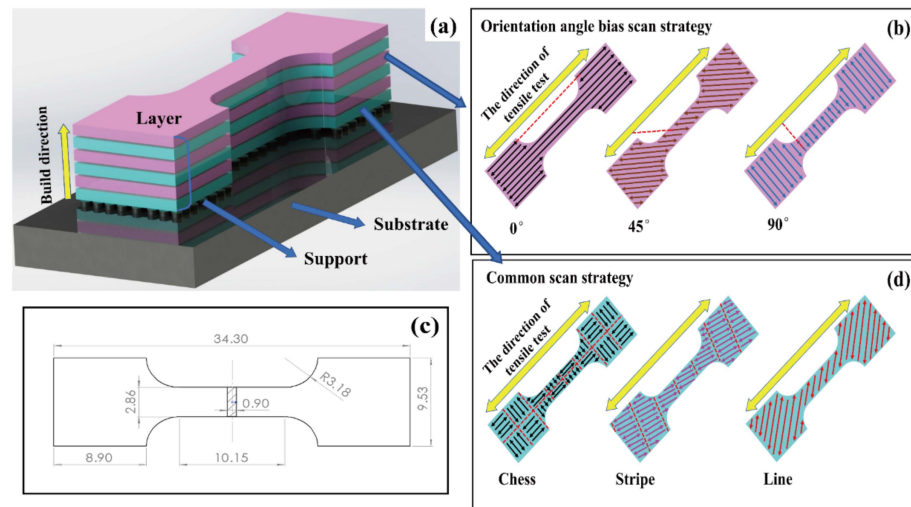| Number	The Combination Method of Different Scan Strategies	Number	The Combination Method of Different Scan Strategies
1	CHESS&0° (C0)	9	STRIPE&45° (S45)
2	CHESS&90° (C90)	10	0°&0° (0°)
3	CHESS&45° (C45)	11	90°&90° (90°)
4	LINE&0° (L0)	12	45°&45° (45°)
5	LINE&90° (L90)	13	LINE (L)
6	LINE&45° (L45)	14	CHESS (C)
7	STRIPE&0° (S0)	15	STRIPE (S)
8	STRIPE&90° (S90)		

Figure 2. Schematic diagram of the combination of different scanning strategies and the tensile specimen dimensions. (**a**) Schematic diagram of the stacking of different forming layers; (**b**) schematic diagram of the scanning strategy for the directional angle-offset shaping layer; (**c**) L-PBF tensile specimen dimensions; (**d**) schematic diagram of the general scanning strategy shaping layer.

The schematic diagram of the combination of different scanning strategies is shown in Figure 3.
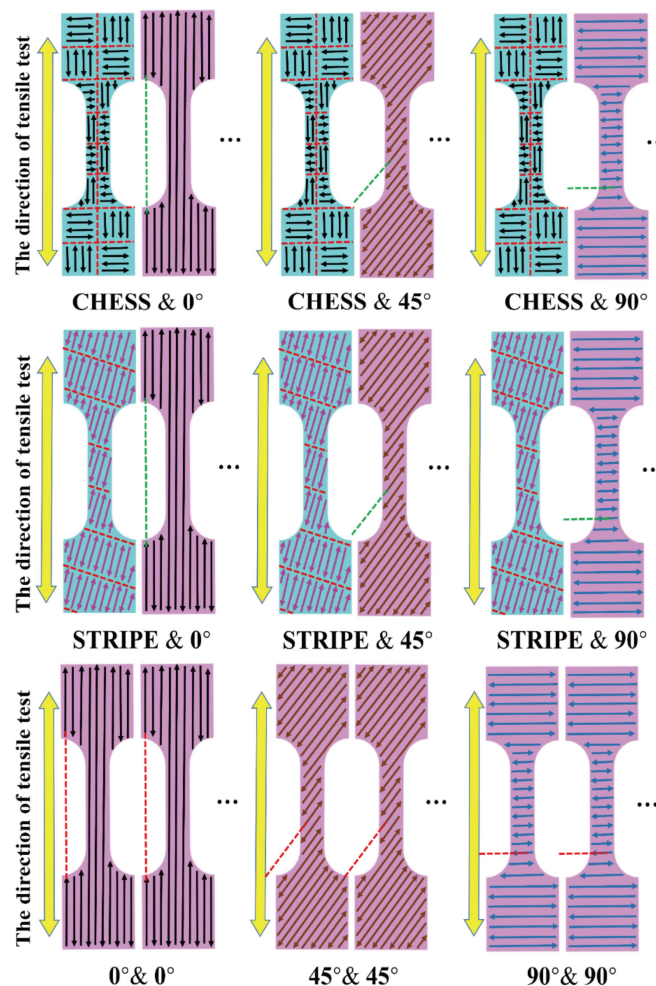

Figure 3. The schematic diagram of the combination of different scanning strategies.

The tensile specimen formed by L-PBF was placed under the KEYENCE three-dimensional field microscope (VHX-600E) to observe the surface morphology of the specimen. The actual L-PBF specimen is shown in Figure 4. The samples' tensile fracture morphology and defects were observed with a desktop scanning electron microscope (Phenom XL). The tensile experiment was carried out on the samples using the electronic universal testing machine (UTM5305) with a machine cross-head speed of 0.01 mm/s. The surface topography of different samples was acquired by scanning with a laser confocal device, and the corresponding surface roughness (Sa) value was obtained. The density of the sample was measured using the Archimedes drainage method, and the average value was measured five times [32]. The surface hardness of the sample was measured with an automatic micro-Vickers hardness tester (TIME6610AT) with a load force of 4.9 N (duration of the 20 s). The average value was taken from three measurements after grinding with sandpaper. Before observing the sample's microstructure under the metallographic microscope (Olympus, bx51m), the sample was etched with standard Kroll reagent (HF:HNO$_3$:H$_2$O = 2:6:92) for 90 s, and then ultrasonically cleaned for 10 min.
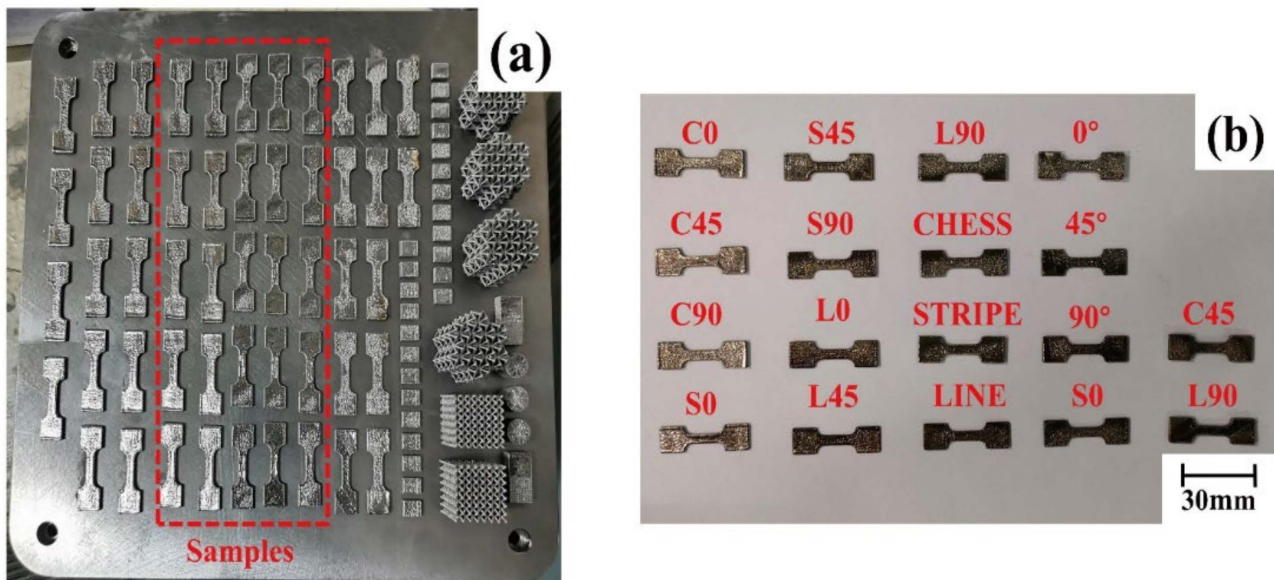

Figure 4. L-PBF forming tensile specimen. (**a**) L-PBF forming sample; (**b**) the actual L-PBF tensile specimen after high-speed wire cutting.

3. Results and Discussion

3.1. Surface Topography

Figure 5 shows the surface macro-morphologies of different L-PBF samples. The results show that, in terms of scanning strategy combination, the CHESS scanning strategy combination had the smoothest surface, a continuous melt channel, and good overlap, as shown in Figure 5a–c. One the other hand, the sample's surface combined with the LINE scanning strategy was uneven, and the melt channel had large fluctuations, as shown in Figure 5g–i. The surface flatness of the S0, S90, and S45 samples was lower than that of the C0, C45, and C90 samples. There were some collapsed areas on the surface, as shown in Figure 5d–f. The samples with poor surface flatness were the L0–L45 sample, which had intermittent melt channels and poor overlap between the melt channels, and the collapse area was further expanded.
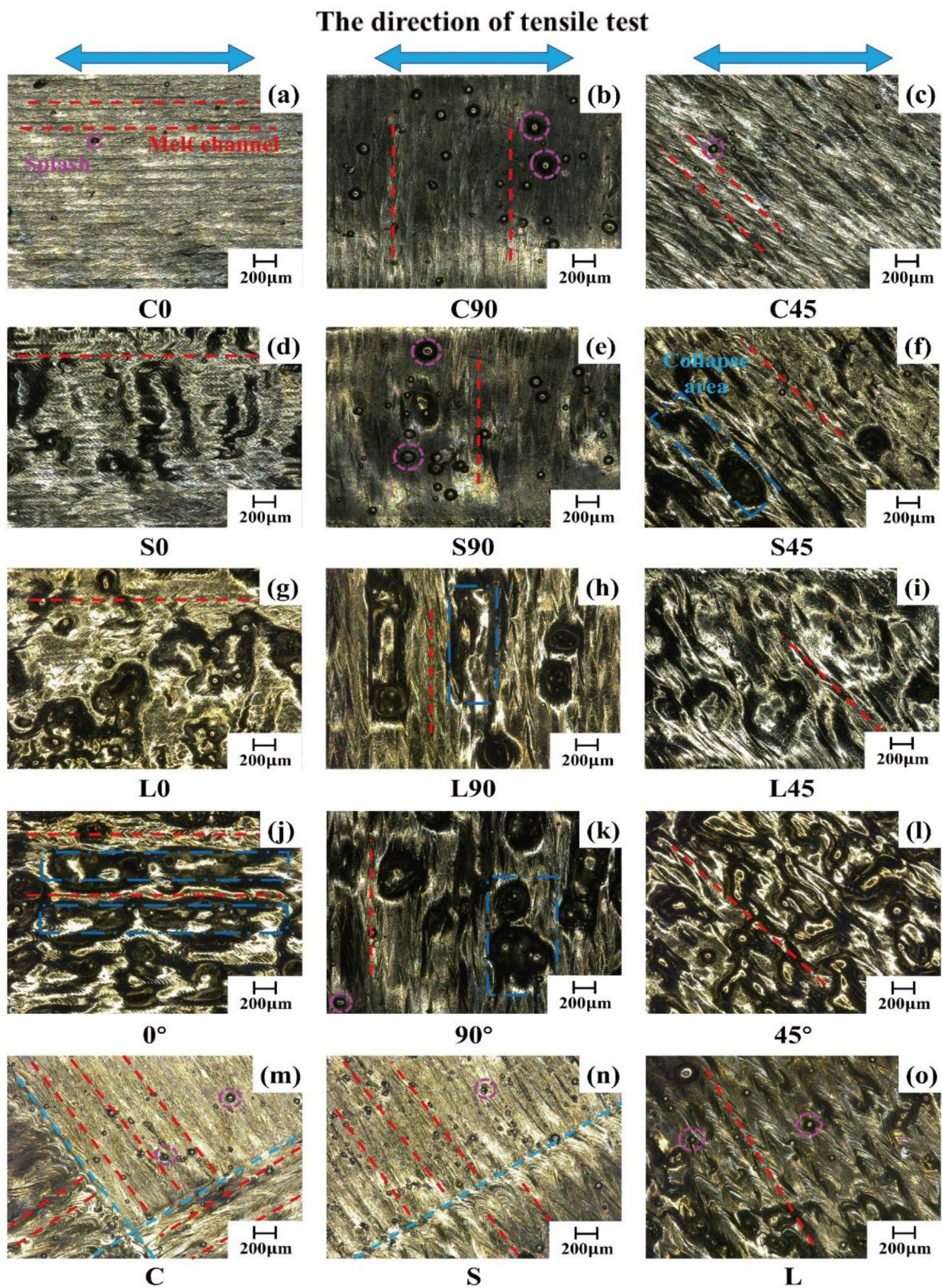
Figure 5. Macroscopic topography of different L-PBF samples. (**a–o**) Corresponding to the surface topography of C0, C90, C45, S0, S90, S45, 0, L90, L45, 0°, 90°, 45°, C, S, and L samples, respectively.

From the offset angle analysis, the L-PBF specimen's surface with 0° and 45° angle offset was flatter and less collapsed than that of the 90° specimen. Because the distance of each scanning line was shorter, the mutual influence between each melt channel was larger. The laser interacted violently with the metal powder bed, resulting in more splashes when the offset angle was 90°, as shown in Figure 5b,e. The distance of each scan line increased, the molten metal powder could be fully flowed and cooled, the spatter was less, and the surface became smoother when the offset angle was 0° and 45°, as shown in Figure 5a,c,d,f.

On the whole, the surface of the L-PBF specimen after the combination of scanning strategies was generally better than that of the single scanning strategy, as shown in Figure 5a–c,j–o. The C (CHESS) scanning strategy can reduce the heat accumulation of L-PBF forming and generate less residual tensile stress, and the forming layers are bonded well [33], which explains why the surface of the C0–C45 samples and the CHESS specimen was flat. The L (LINE) scanning strategy was more similar to the scanning path of the angular offset layer, and thus it may cause overlap between the scanning lines, increase the heat accumulation, hinder the cooling of the melt, and result in a rough surface in the sample. The poor bonding between the forming layers resulted in localized collapsed areas on the surface, which also explained the worst surface of the 0°–45° specimen, as shown in Figure 5j–l.

3.2. Surface Roughness

Figure 6 shows the surface roughness (Sa) of different L-PBF samples. The results demonstrated that among all scanning strategies, the surface roughness of the sample with the CHESS combination scanning strategy was the lowest, and the surface roughness of the CHESS&45° sample under this strategy was 14 μm, which was the lowest value under this scanning strategy. The surface roughness value of the sample was the highest with the combined LINE scanning strategy, and the surface roughness value of the LINE&90° sample was the highest, reaching 42 μm. Overall, under a specific general scanning strategy, the increase in the angle offset improves the surface roughness value of the sample to a certain extent. This phenomenon may be because the increase in the offset angle reduces the distance of a single laser scan; the laser acts on the sample's surface more frequently, accumulates more heat, and thus causes a higher temperature gradient. As a result, defects such as spattering increase significantly on the surface of the sample, and the surface roughness value rises, as shown in Figure 6. Compared with the LINE scan strategy, the surface roughness of the formed sample was lower with the CHESS scan strategy. The reason was that the CHESS scanning strategy could reduce heat accumulation and make the heat distribution on the sample surface more uniform [34,35]. The value of surface roughness and defects had been decreased.

To further explore the surface micro-morphology and surface roughness of the sample under the condition of a single scanning strategy, the micro-morphology of the sample was obtained using a laser confocal device, as shown in Figure 7. The results show that the surface roughness value of the samples formed with a single scanning strategy was relatively higher than that of the samples formed with different scanning strategies. With the increase in the angle offset, the surface roughness of the samples had an upward trend. Among them, the surface roughness value of the 90° sample was the largest, reaching 83 μm. In addition, the study also found that under the scanning strategy of a single angle offset, corresponding protrusions appeared on the surface of the sample, the direction was parallel to the offset direction, and the width of the melt channel was about 100–200 μm, as shown in Figure 7b. This phenomenon occurred because some gaps would appear in the overlap between each melt track during L-PBF forming. At the same time, the laser scanning path of each forming layer was the same. The gaps continuously accumulated during the stacking process and finally expanded into macroscopic ravines. The direction was the same as the laser scanning direction, as shown in Figure 7c. The surface roughness of the sample was relatively low, around 25 μm under the general scanning strategy. Compared with the scanning strategy of angle offset, the general scanning strategy rotates 67° per

layer, compensating for the gap between the forming layers so that less surface roughness can be obtained, as shown in Figure 7f. However, under the general scanning strategy, the melt channels on the sample's surface were visible and evenly distributed without obvious ravines. The size of the melt channels was maintained at about 100 μm, as shown in Figure 7e. Compared with the single-angle offset scanning strategy, the melting channel bulge width of the general scanning strategy is smaller, and the distribution is uniform without obvious grooves.
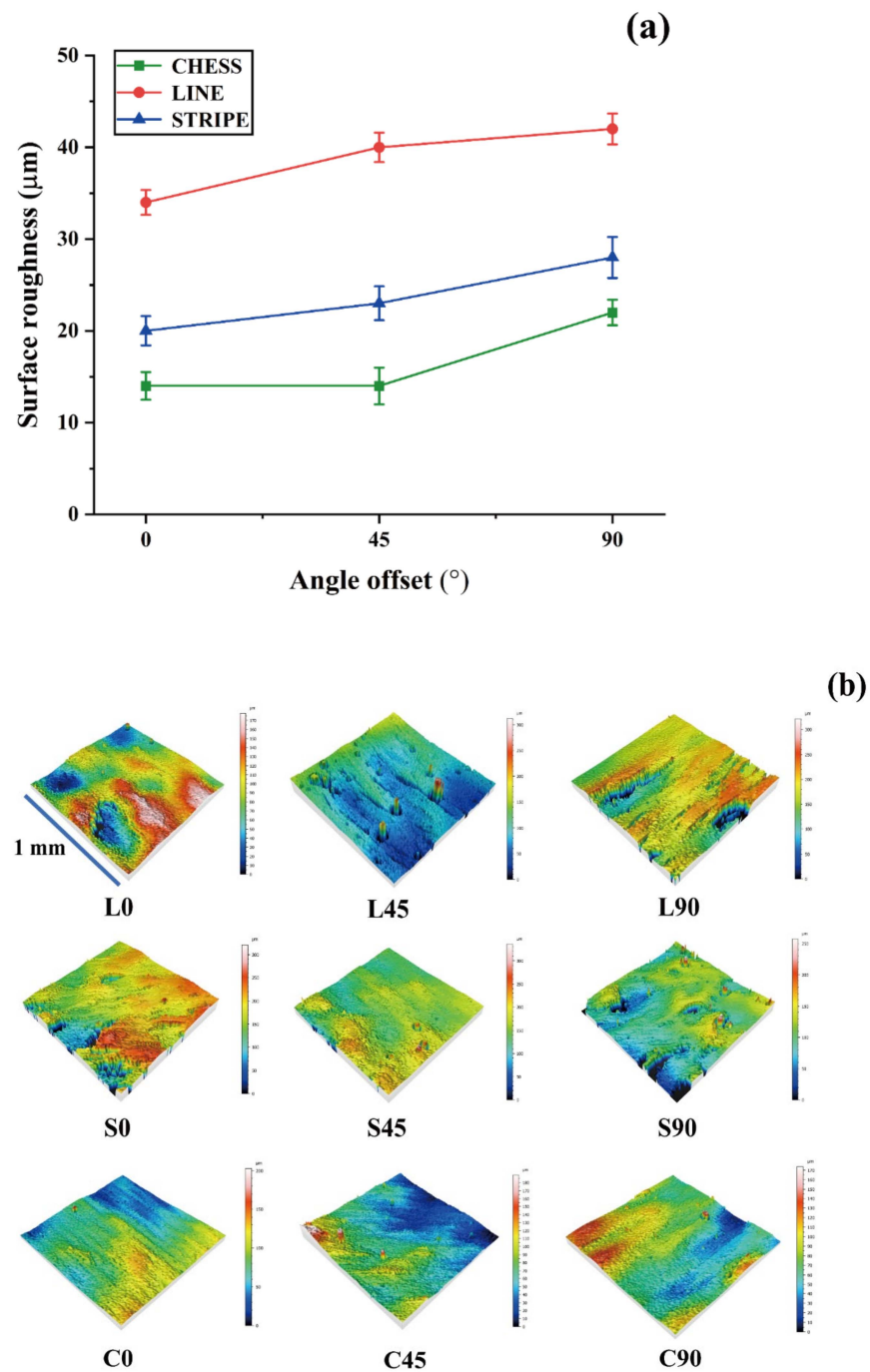

Figure 6. Surface roughness of L-PBF samples under different combinations of scanning strategies. (**a**) Surface roughness of L-PBF samples under different combinations of scanning strategies; (**b**) surface micro-morphologies of samples under different combinations of scanning strategies.
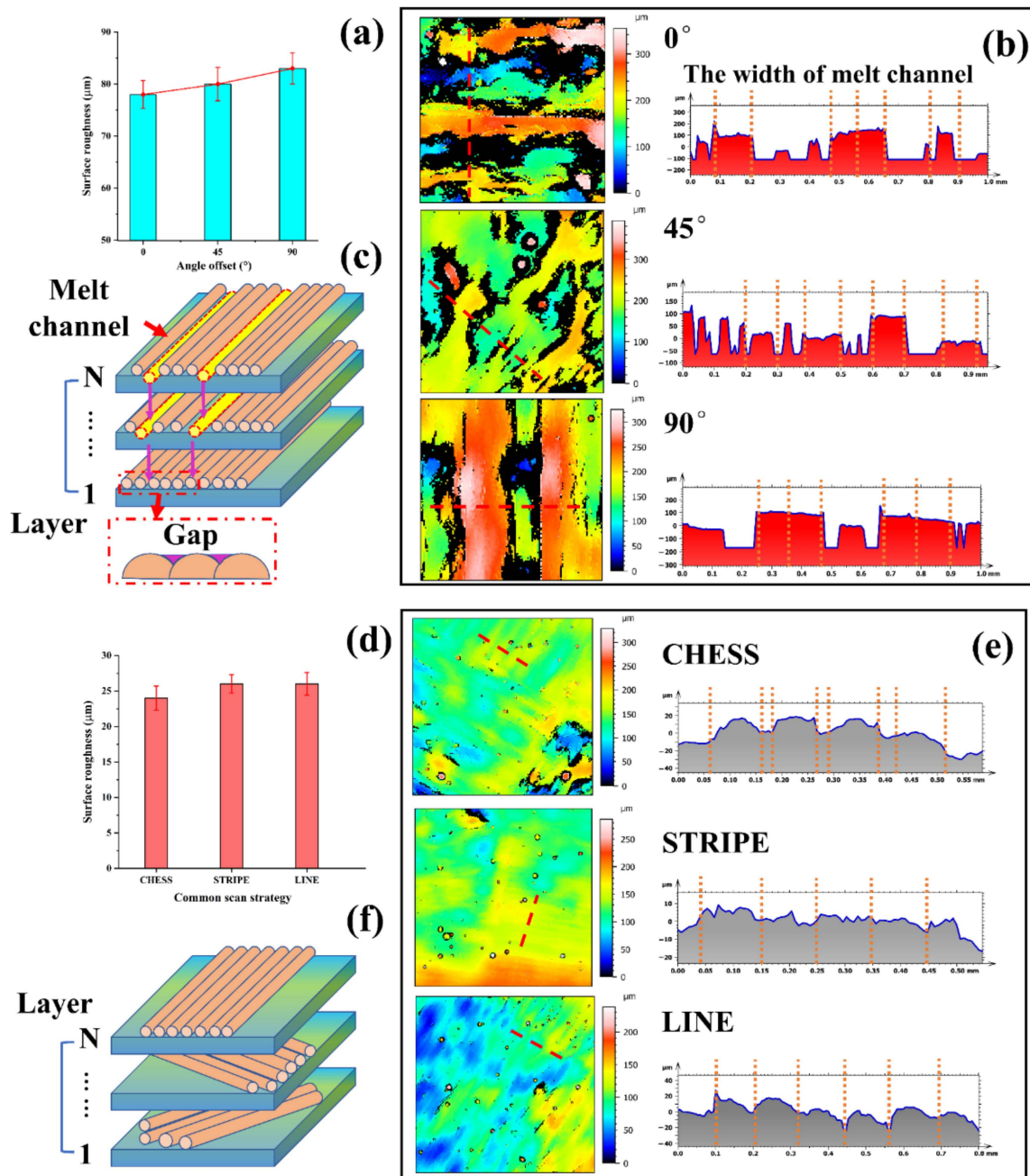
Figure 7. Surface roughness and corresponding cross-sections of L-PBF samples under a single scanning strategy. (**a**) Surface roughness of specimen at angular offset; (**b**) microscopic surface morphology and cross-sectional view of the sample under angular offset; (**c**) schematic diagram of sample surface collapse under angular offset; (**d**) surface roughness of specimen under general scanning strategy; (**e**) microscopic surface topography and cross-sectional view of the sample under the general scanning strategy; (**f**) schematic diagram of sample forming under general scanning strategy.

3.3. Surface Hardness

Figure 8 shows the surface hardness of the L-PBF-formed samples. The results show that the surface hardness of the sample combined with the LINE scanning strategy was the highest, and the surface hardness of the LINE&90° sample was the highest, reaching 409 HV; the surface hardness of the samples combined with the CHESS scanning strategy was the lowest among this scanning strategy. In addition, it was found that the surface hardness was highest under the offset angle of 90° and the LINE scanning strategy, as shown

in Figure 8a. The surface hardness of the sample was generally at a low level under the CHESS scanning strategy, as shown in Figure 8a,c. The L-PBF samples generally have high residual stress because the forming process has the characteristics of a large temperature gradient and rapid cooling rate [36,37]. The residual stress provides the surface hardness of the specimen to a certain extent [38]. The CHESS scanning strategy can reduce the heat accumulation and the temperature gradient, which explains why the surface hardness of the L-PBF samples was generally low under the CHESS scanning strategy, as shown in Figure 8a,c. The surface hardness of the sample was maintained between 400–405 HV under the scanning strategy with a single angle offset, which was generally higher than that of the general scanning strategy. The reason was that the laser continuously scans at the same position, leading to a larger temperature gradient resulting in larger residual stress. Because each layer of LPBBF forming will generate residual stress [39], the residual stress will increase with the superposition of forming layers. The repeated action of the laser increases the residual stress of each forming layer and further improves the surface hardness of the formed sample, as shown in Figure 8b.
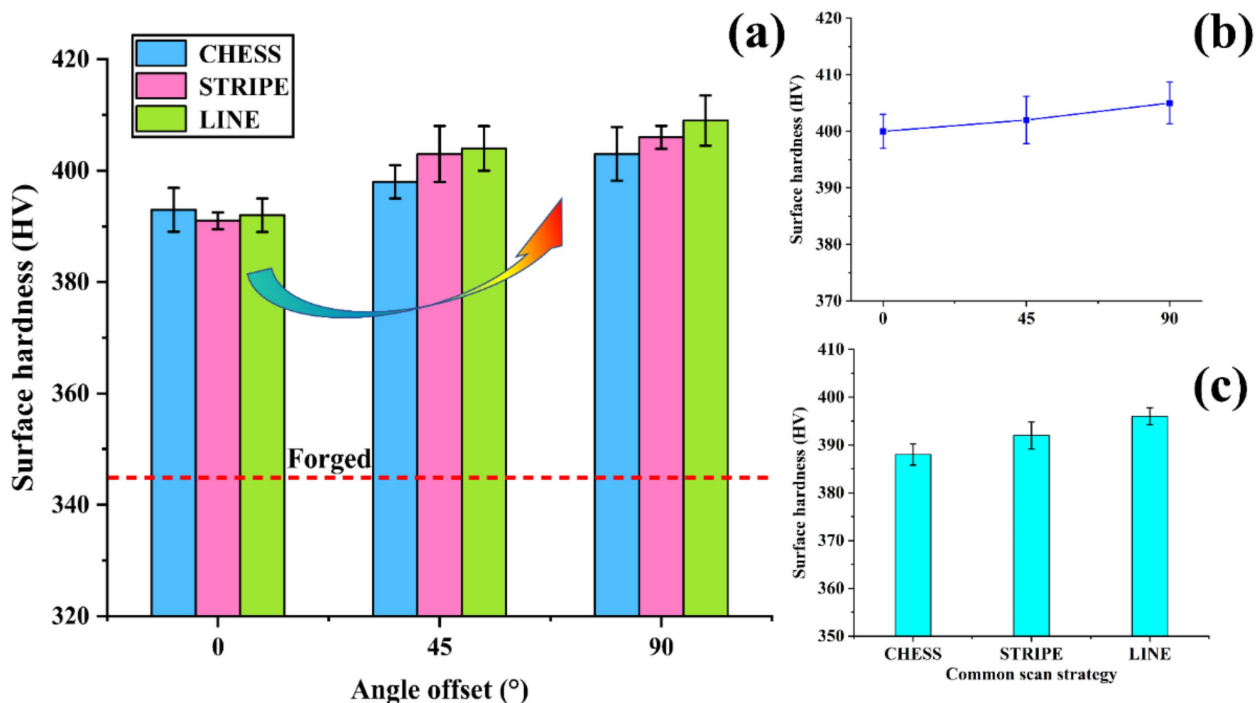

Figure 8. Surface hardness of L-PBF samples under different combinations of scanning strategies and a single scanning strategy. (**a**) Surface hardness of samples under different combinations of scanning strategies; (**b**) surface hardness of samples under angled offset scanning strategy; (**c**) surface hardness of samples under general scanning strategy.

3.4. Mechanical Properties

The results of the tensile experiment on different L-PBF samples are shown in Figure 9. The results show that under the combination of the general scanning strategy and the angle-offset scanning strategy, the tensile properties of the CHESS scanning strategy combination were the highest. Among them, the CHESS&45° specimen had the best tensile properties, with a tensile strength of 1125 MPa, a yield strength of 912 MPa, and an elongation of 8.2%; the tensile properties of the LINE scanning strategy combination specimen were the lowest, in which the tensile strength of the LINE&90° specimen was only 810 MPa. Overall, the tensile properties of the samples combined with the CHESS scanning strategy were the best, and the tensile strengths were all higher than 900 MPa, as shown in Figure 9a. From the general scanning strategy, the CHESS scanning strategy had the best tensile performance,

reaching a tensile strength of 1003 MPa, as shown in Figure 9c. From the angle-offset scanning strategy, the 45° scanning strategy had the best tensile performance, reaching a tensile strength of 715 MPa, as shown in Figure 9b. The performance of the CHESS&45° scanning strategy combined specimen was greater than that of the single scanning strategy specimen. Compared with the CHESS scanning strategy and the 45° scanning strategy, the tensile performance of the samples under the CHESS&45° scanning strategy was improved by 12.8% and 57.3%, respectively. Compared with the research of other scholars, the comprehensive performance of this test sample is better, as shown in Table 4.
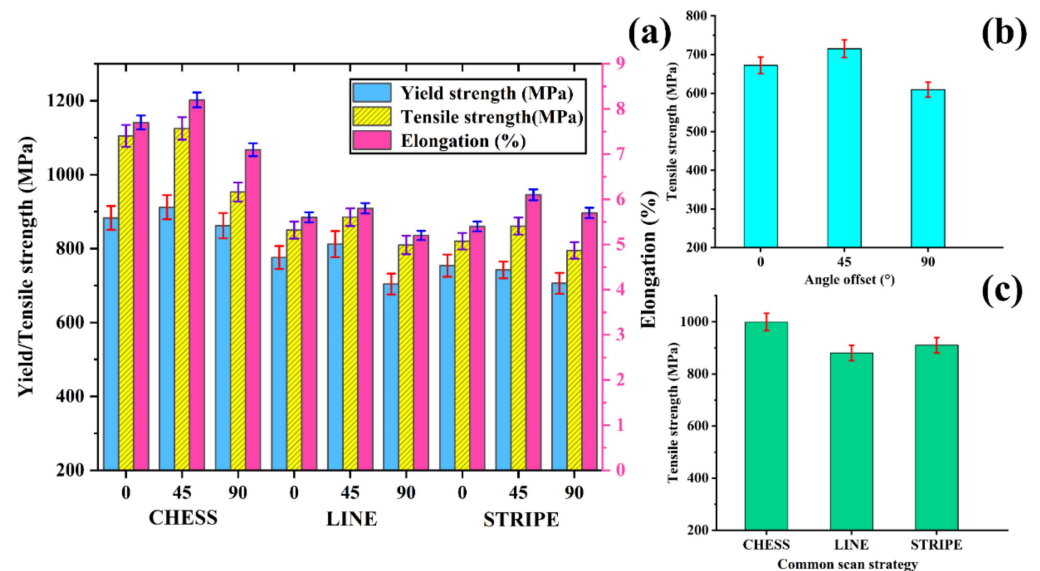

Figure 9. Tensile properties of L-PBF samples under different combinations of scanning strategies and a single scanning strategy. (**a**) Tensile properties of L-PBF samples under various combinations of scanning strategies; (**b**) tensile properties of L-PBF samples under angled offset scanning strategy; (**c**) tensile properties of L-PBF samples under general scanning strategy.

Table 4. Some other experimental studies on the tensile properties of L-PBF-formed TC4 titanium alloy specimens.

References	Manufacturing Means	Yield Strength (MPa)	Ultimate Tensile Stress (MPa)	Elongation (%)
[40]	As fabricated	937	1107	7.3
[41]	As fabricated	-	1188	9.5
[42]	As fabricated	969	1087	11.3
[43]	As fabricated	1021	1200	2.23
[44]	As fabricated	968	1013	3.2
In this research	As fabricated	912	1125	8.2

To further explore the tensile conditions of the L-PBF samples under different combinations of scanning strategies and single scanning strategies, the fractures of the tensile samples were analyzed, as shown in Figure 10. The results show that the samples combined with the CHESS scanning strategy were mainly ductile fractures, with a certain amount of dimple structure and step-like slip separation, which was also the reason for the higher elongation of the C0 specimen, as shown in Figure 10a. The fractures of the C45 and C90 samples were mainly ductile fractures, with many dimple structures. Compared with C90 samples, the dimple structure of C45 samples was more obvious, so the tensile strength and elongation of C45 samples were higher, as shown in Figure 10b,c. From the single scanning strategy aspect, the CHESS strategy also had the phenomenon of slip separation, which explained the higher elongation of the CHESS strategy samples, as shown in Figure 10d.

The STRIPE strategy had many quasi-cleavage fractures accompanied by a particular brittle fracture, as shown in Figure 10e. At the same time, the LINE sample presented a brittle fracture with a relatively smooth and neat section, as shown in Figure 10f. In addition, some delamination phenomena were found in the tensile fracture of the samples under a single angle offset, as shown in Figure 10g–i. Different internal porosity and anisotropic microstructures result from the heating and cooling rate during SLM forming [45]. However, under the single-angle offset scanning strategy, the heat accumulation during formation is greater, and the temperature gradient is greater, resulting in delamination between the forming layers, thereby reducing the sample's mechanical properties. The samples had a certain number of dimple structures, and brittle sections indicated that the fracture mode of the samples was a quasi-cleavage fracture.
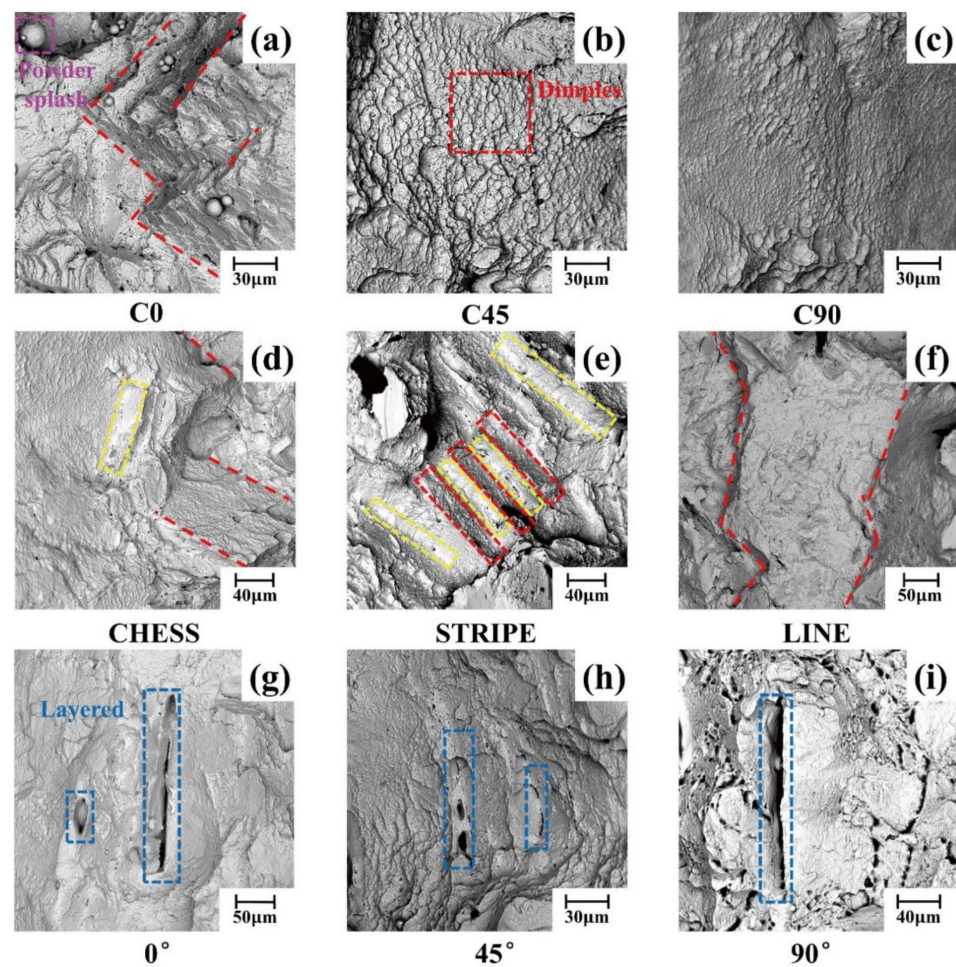

Figure 10. Tensile fracture morphologies of L-PBF samples under different combinations of scanning strategies and a single scanning strategy. (**a**–**c**) Tensile fracture morphologies of C0, C45, and C90 samples; (**d**–**f**) CHESS, STRIPE, LINE single scanning strategy sample tensile fracture morphology; (**g**–**i**) tensile fracture morphologies of samples with single scanning strategy at 0°, 45°, and 90°.

3.5. Density

The L-PBF sample's density is shown in Figure 11. The results show that the density of the samples was the highest under the combination of CHESS scanning strategies, and the C0 sample had the highest density, reaching 99.88%. The density of the samples combined with the LINE scanning strategy was the lowest, and the lowest density of the L90 sample was 96%, as shown in Figure 11a. The possible reason for this phenomenon was that the forming layers of the sample under the CHESS strategy and the angle offset strategy were better combined, and there were fewer interlayer pores, so the forming density of the

sample was higher. From the point of view of the single scanning strategy, the sample density of the single angle offset scanning strategy was generally low, with an average of about 92%, as shown in Figure 11b. This was due to the collapse of the melt channel and poor fusion between the layers during L-PBF forming. The density of the general scanning strategy was at a relatively high level, averaging around 99%, which was due to the increasing scanning angle between the forming layers, compensating for the voids in the melt channel. At the same time, the heat accumulation and temperature gradient were reduced, resulting in better bonding between the forming layers, as shown in Figure 11b.
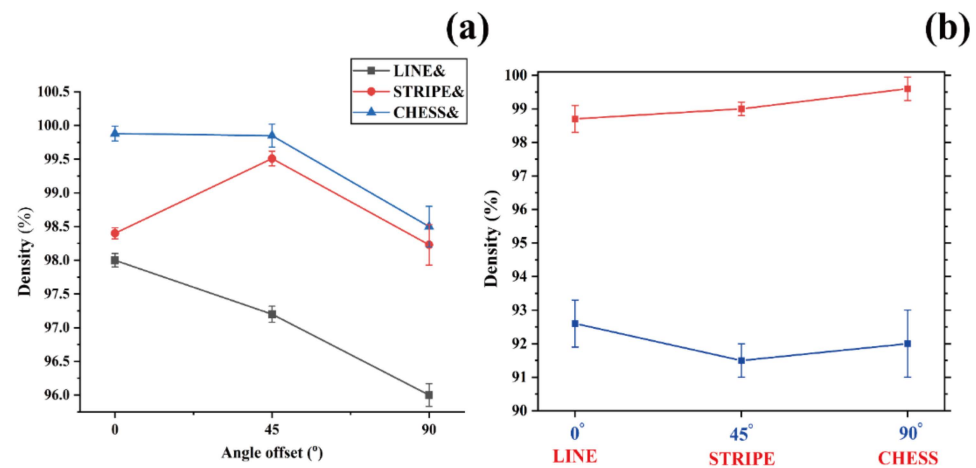

Figure 11. The density of L-PBF samples under different combinations of scanning strategies and a single scanning strategy. (**a**) The density of L-PBF samples under various combinations of scanning strategies; (**b**) the density of samples under angular offset scanning and general scanning strategies.

3.6. Microstructure

The microstructures of different L-PBF samples are shown in Figure 12. The results show that the microstructure of the L-PBF samples was mainly the primary β phase and α′ martensite phase. Nevertheless, the composition and distribution had specific differences under different scanning strategies. The microstructure distribution of the CHESS scanning strategy combination sample was uniform, and the melt channel was visible. A certain number of columnar β-crystals were distributed in the longitudinal section, and the grain boundaries were clear and uniformly distributed. From the analysis of the combination of scanning strategies, there were no holes on the upper surface of the C0–C90 sample, the melt channel was clear, and the distribution of each phase was uniform, as shown in Figure 12a–c. However, under the angle-offset scanning strategy, the upper surface of the sample had some holes, and the melt channel was unclear. When the angle offset was 0°, the size of the pores on the surface of the sample was smaller, while when the angle offset was 45°, the size of the pores was larger and accompanied by a certain number of cracks; when the angle offset was 90°, the size of the pores was further increased, and their distribution was paralleled to the offset angle, as shown in Figure 12d–f. The longitudinal microstructure of the sample is shown in Figure 12g–r. It was found that a certain number of columnar β crystals were distributed in the longitudinal section of the C0–C90 sample, which was paralleled to the build direction. In addition, the forming layers were bonded with clear boundaries well, the columnar β-crystals grew continuously, and the grain boundaries were visible, as shown in Figure 12g–i,p–r. Among them, the columnar β-crystal size of the C45 sample was relatively coarse, which enhanced the sample's tensile strength, as shown in Figure 12h. Under the general scanning strategy, the columnar β grain boundaries were unclear. The growth was interrupted; the boundaries between the forming layers were blurred, and there were tiny gaps between the layers, as shown in Figure 12j–l. Some severe delamination occurred in the sample under the angle-offset scanning strategy, which was also the reason for the low density of the piece, as shown in Figure 12m–o. It was found that when the angle offset was 45° and 90°, the columnar β-crystal growth of the

sample was seriously hindered due to the severe delamination phenomenon. The crystals were laterally staggered, and the growth was interrupted. This led to a decrease in the mechanical properties of the specimen, and the delamination phenomenon also made the specimen surface more uneven, as shown in Figure 12n–o.
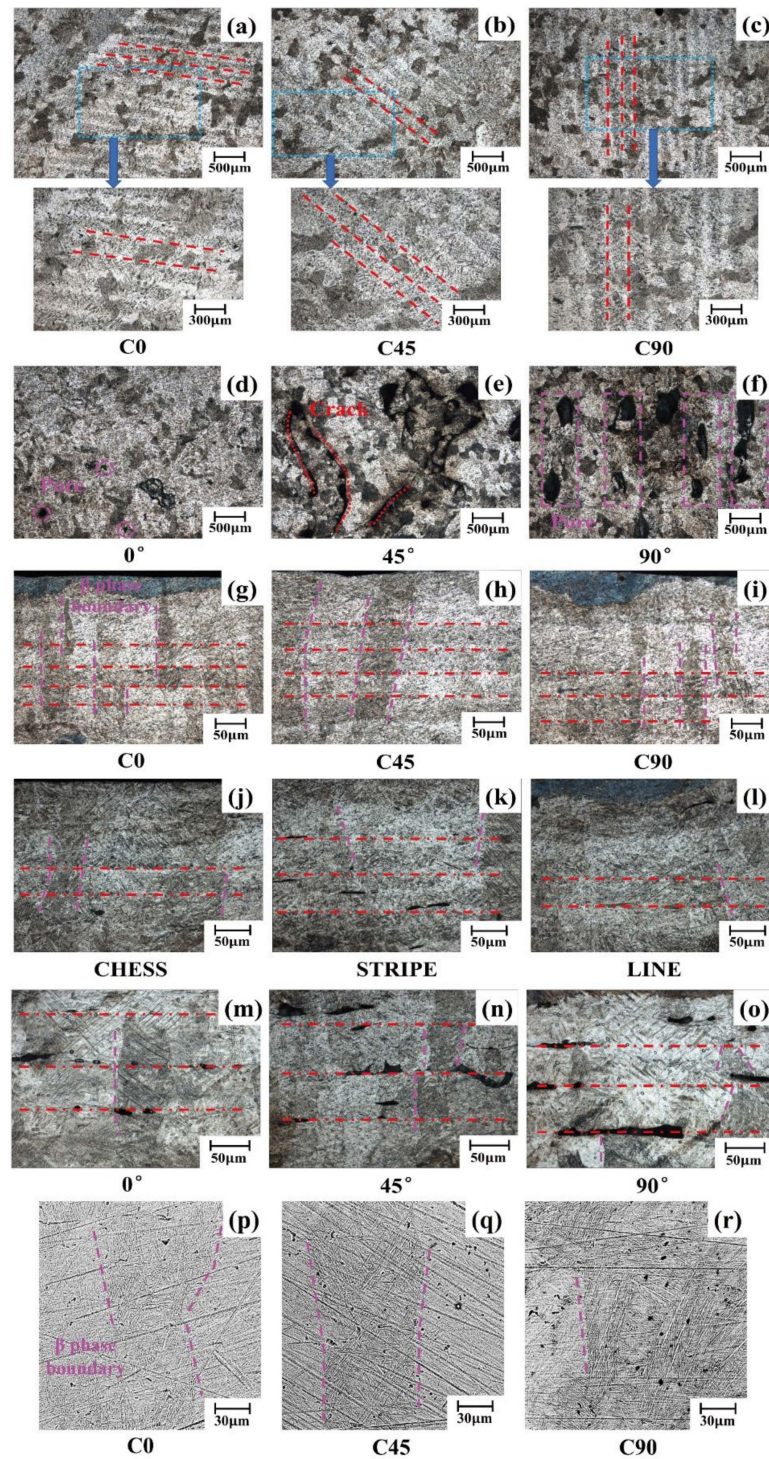

Figure 12. Metallographic structure of L-PBF samples under different combinations of scanning strategies and a single scanning strategy. (**a**–**f**) Corresponding to the upper-surface metallographic structure of the C0, C45, C90, 0°, 45°, and 90° samples, respectively; (**g**–**o**) corresponding to the longitudinal-section metallographic structure of C0, C45, C90, CHESS, STRIPE, LINE, 0°, 45°, and 90° samples respectively; (**p**–**r**) SEM images of C0, C45, and C90 samples.

4. Conclusions

In this experiment, LINE scanning, CHESS scanning, and STRIPE scanning strategies combined with a directional angle offset scanning strategy were studied to explore the surface quality, mechanical properties, and microstructure of L-PBF samples with different scanning strategies. Our intention was for the optimal combination method to directionally enhance the mechanical properties of a TC4 titanium alloy with better surface quality. The conclusions are as follows:

The surface of the L-PBF specimen under the CHESS scanning strategy combination was relatively flat, and the surface roughness was the lowest. The surface roughness of the CHESS&45° scanning strategy combination was the lowest, reaching 14 μm. The sample's surface collapsed under the scanning strategy with a single angular offset, and the protruding melt channel was parallel to the angular offset direction. Due to the repeated action of the laser on the surface of the sample, the voids between the melt channels were continuously accumulated and enlarged, resulting in the collapse of the sample's surface.

The surface hardness of the samples was generally higher with the LINE scanning strategy and the angle offset of 90°, and the highest hardness combination was LINE&90°, reaching 409 HV, which was much higher than that of the forgings. The overall surface hardness of the samples combined with the CHESS scanning strategy was the lowest because the CHESS scanning strategy could reduce heat accumulation, reduce the temperature gradient, and generate less residual tensile stress and lower surface hardness.

The tensile properties of the L-PBF samples were the best under the combination of CHESS scanning strategies. Among them, the tensile properties of the sample were the best under the combination of CHESS&45°: the tensile strength reached 1125 MPa, the yield strength was 912 MPa, and the elongation was 8.2%. The fracture mode of the sample was a ductile fracture, and there were many dimple structures in the fracture. The performance of the CHESS&45° scanning strategy combined specimen was greater than that of the single scanning strategy formed specimen. Compared with the CHESS scanning strategy, the tensile performance was improved by 12.8%. Compared with the 45° scanning strategy sample, the tensile performance was improved by 57.3%, which enhanced the tensile properties of the sample to a certain extent.

The density of the L-PBF samples was higher under the combination of the CHESS scanning strategy, among which the sample density of the CHESS&0° combination was the highest, reaching 99.88%. The microstructure of the L-PBF sample mainly included the primary β phase and α′ martensite phase. The upper surface of the CHESS scanning strategy combination sample had a clear melt channel, and the distribution of each phase was uniform. A certain number of columnar β-crystals were distributed in the longitudinal section paralleled to the build direction, and the columnar β-crystals of CHESS&45° were relatively coarse.

Author Contributions: W.S.: conceptualization, resources, investigation, methodology, formal analysis, writing—original draft, writing—review and editing; J.L.: validation, writing, writing—original draft, reviewing and editing, writing—review and editing; Y.J.: conceptualization, investigation, validation, visualization, writing—original draft; Y.L. (Yude Liu): conceptualization, investigation, methodology, validation, visualization, investigation, resources; Y.L. (Yuxiang Lin): conceptualization, investigation, methodology, validation, visualization; Y.H.: conceptualization, investigation, methodology, validation, visualization. All authors have read and agreed to the published version of the manuscript.

Institutional Review Board Statement: Not applicable.

Informed Consent Statement: Not applicable.

Data Availability Statement: All data from this study were presented in this paper.

Conflicts of Interest: The authors declare that they have no conflict of interest.

References

1. Ivanova, T.; Mashlan, M.; Ingr, T.; Doláková, H.; Sarychev, D.; Sedláčková, A. Mössbauer Spectroscopy for Additive Manufacturing by Selective Laser Melting. *Metals* **2022**, *12*, 551. [CrossRef]
2. Li, C.; Sun, J.; Feng, A.; Wang, H.; Zhang, X.; Zhang, C.; Zhao, F.; Cao, G.; Qu, S.; Chen, D. Active Slip Mode Analysis of an Additively Manufactured Ti-6Al-4V Alloy via In-Grain Misorientation Axis Distribution. *Metals* **2022**, *12*, 532. [CrossRef]
3. Lovašiová, P.; Lovaši, T.; Kubásek, J.; Jablonská, E.; Msallamová, Š.; Michalcová, A.; Vojtěch, D.; Suchý, J.; Koutný, D.; Ghassan Hamed Alzubi, E. Biodegradable WE43 Magnesium Alloy Produced by Selective Laser Melting: Mechanical Properties, Corrosion Behavior, and In-Vitro Cytotoxicity. *Metals* **2022**, *12*, 469. [CrossRef]
4. Zhao, Z.; Wang, H.; Huo, P.; Bai, P.; Du, W.; Li, X.; Li, J.; Zhang, W. Effect of Solution Temperature on the Microstructure and Properties of 17-4PH High-Strength Steel Samples Formed by Selective Laser Melting. *Metals* **2022**, *12*, 425. [CrossRef]
5. Zhang, M.; Zhang, B.; Wen, Y.; Qu, X.H. Research progress on selective laser melting processing for nickel-based superalloy. *Int. J. Adv. Manuf. Technol.* **2022**, *29*, 369–388. [CrossRef]
6. Wang, Y.; Guo, Y.Y.; Jin, Y.B.; Wang, Y.J.; Wang, C. Mechanical properties, corrosion resistance, and anti-adherence characterization of pure titanium fabricated by casting, milling, and selective laser melting. *J. Biomed. Mater. Res. Part B Appl. Biomater.* **2022**, *110*, 1523–1534. [CrossRef]
7. Guo, Y.T.; Xu, Z.Z.; Qi, W.; Zu, S.; Liu, M.Q.; Yu, Z.L.; Zhang, Z.H.; Ren, L.Q. Corrosion resistance and biocompatibility of graphene oxide coating on the surface of the additively manufactured NiTi alloy. *Prog. Org. Coat.* **2022**, *164*, 106722. [CrossRef]
8. Lee, W.F.; Wang, J.C.; Hsu, C.Y.; Peng, P.W. Microstructure, mechanical properties, and retentive forces of cobalt-chromium removable partial denture frameworks fabricated by selective laser melting followed by heat treatment. *J. Prosthet. Dent.* **2022**, *127*, 115–121. [CrossRef]
9. Zhai, W.; Zhou, W.; Zhu, Z.G.; Nai, S.M.L. Selective Laser Melting of 304L and 316L Stainless Steels: A Comparative Study of Microstructures and Mechanical Properties. *Steel Res. Int.* **2022**, 2100664. [CrossRef]
10. Vaverka, O.; Koutny, D.; Palousek, D. Topologically optimized axle carrier for Formula Student produced by selective laser melting. *Rapid Prototyp. J.* **2019**, *25*, 1545–1551. [CrossRef]
11. Akbay, Ö.C.; Bahçe, E.; Uysal, A.; Gezer, I. Production and Cleaning of Lattice Structures Used in the Space and Aerospace Industry with Metal Additive Manufacturing Method. *J. Mater. Eng. Perform.* **2022**, *136*, 1–12. [CrossRef]
12. Kurzynowski, T.; Pawlak, A.; Smolina, I. The potential of SLM technology for processing magnesium alloys in aerospace industry. *Arch. Civ. Mech. Eng.* **2020**, *20*, 23. [CrossRef]
13. Peng, P.W.; Hsu, C.Y.; Huang, H.Y.; Chao, J.C.; Lee, W.F. Trueness of removable partial denture frameworks additively manufactured with selective laser melting. *J. Prosthet. Dent.* **2022**, *127*, 122–127. [CrossRef]
14. Dobrzański, L.A.; Dobrzański, L.B.; Achtelik-Franczak, A.; Dobrzańska, J. Application Solid Laser-Sintered or Machined Ti6Al4V Alloy in Manufacturing of Dental Implants and Dental Prosthetic Restorations According to Dentistry 4.0 Concept. *Processes* **2020**, *8*, 664. [CrossRef]
15. Mustafa, G.; Samed, E.; Mesut, B.; Alper, T.; Hakan, Y. The strain rate sensitive flow stresses and constitutive equations of a selective-laser-melt and an annealed-rolled 316L stainless steel: A comparative study. *Mater. Sci. Eng. A* **2022**, *838*, 142743.
16. Naujokat, H.; Gökkaya, A.I.; Açil, Y.; Klaas, L.; Tim, K.; Sabine, F.; Jörg, W. In vivo biocompatibility evaluation of 3D-printed nickel–titanium fabricated by selective laser melting. *J. Mater. Sci. Mater. Med.* **2022**, *33*, 13. [CrossRef]
17. Dylan, A.; Kyriakos, K.I.; Wallbrink, C.; Song, T. Cyclic plasticity and microstructure of as-built SLM Ti-6Al-4V: The effect of build orientation. *Mater. Sci. Eng. A* **2017**, *701*, 85–100.
18. Zhang, J.Q.; Wang, M.J.; Liu, J.Y.; Niu, L.H.; Wang, J.H. Influence of scanning strategy on printing quality and properties of selective laser melted 18Ni300 maraging steel. *J. Mater. Eng.* **2020**, *48*, 105–113.
19. Cao, X.; Carter, L.N.; Villapún, V.M.; Cantaboni, F.; De Sio, G.; Lowther, M.; Louth, S.E.T.; Grover, L.; Ginestra, P.; Cox, S.C. Optimisation of single contour strategy in selective laser melting of Ti-6Al-4V lattices. *Rapid Prototyp. J.* **2022**, *28*, 907–915. [CrossRef]
20. Nespoli, A.; Bennato, N.; Villa, E.; Passaretti, F. Study of anisotropy through microscopy, internal friction and electrical resistivity measurements of Ti-6Al-4V samples fabricated by selective laser melting. *Rapid Prototyp. J.* **2022**, *28*, 1060–1075. [CrossRef]
21. Khorasani, A.M.; Gibson, I.; Ghasemi, A.; Ghaderi, A. Modelling of laser powder bed fusion process and analysing the effective parameters on surface characteristics of Ti-6Al-4V. *Int. J. Mech. Sci.* **2020**, *168*, 105299. [CrossRef]
22. Wang, P.; Chen, D.; Fan, J.; Sun, K.; Wu, S.; Li, J.; Sun, Y. Study on the influence of process parameters on high performance Ti-6Al-4V parts in laser powder bed fusion. *Rapid Prototyp. J.* **2022**. [CrossRef]
23. Yan, Z.Y.; Zhou, Q.J.; Hou, Y.F.; Yang, G.W.; Ma, C.Q.; Wang, F.D. Effect of Interlayer Residence Time on Microstructures and Mechanical Properties of Laser Melting Deposited TC11 Titanium Alloys. *Chin. J. Lasers* **2018**, *45*, 44–51.
24. Cen, W.H.; Tang, H.L.; Zhang, J.Z.; Yuan, G.X.; Yan, H.H.; Long, Y. Scanning Strategy to Improve the Overlapping Quality of Partition in Selective Laser Melting. *Chin. J. Lasers* **2021**, *48*, 173–183.

25. Zou, S.; Xiao, H.B.; Ye, F.P.; Li, Z.C.; Tang, W.Z.; Zhu, F.; Chen, C.T.; Zhu, C. Numerical analysis of the effect of the scan strategy on the residual stress in the multi-laser selective laser melting. *Results Phys.* **2020**, *16*, 103005. [CrossRef]

26. Yu, W.H.; Sing, S.L.; Chua, C.K.; Tian, X.L. Influence of re-melting on surface roughness and porosity of AlSi10Mg parts fabricated by selective laser melting. *J. Alloys Compd.* **2019**, *792*, 574–581. [CrossRef]

27. Li, X.F.; Yi, D.H.; Wu, X.Y.; Zhang, J.F.; Yang, X.H.; Zhao, Z.X.; Feng, Y.H.; Wang, J.H.; Bai, P.K.; Liu, B.; et al. Effect of construction angles on microstructure and mechanical properties of AlSi10Mg alloy fabricated by selective laser melting. *J. Alloys Compd.* **2021**, *881*, 160459. [CrossRef]

28. Rashid, R.; Masood, S.; Ruan, D.; Palanisamy, S.; Brandt, M. Effect of scan strategy on density and metallurgical properties of 17-4PH parts printed by Selective Laser Melting (SLM). *J. Mater. Process. Technol.* **2017**, *249*, 502–511. [CrossRef]

29. Rashid, R.; Masood, S.; Ruan, D.; Palanisamy, S.; Elambasseril, J.; Brandt, M. Effect of energy per layer on the anisotropy of selective laser melted AlSi12 aluminium alloy. *Addit. Manuf.* **2018**, *22*, 426–439. [CrossRef]

30. Cottam, R.; Palanisamy, S.; Avdeev, M.; Jarvis, T.; Henry, C.; Cuiuri, D.; Balogh, L.; Abdul Rahman Rashid, R. Diffraction Line Profile Analysis of 3D Wedge Samples of Ti-6Al-4V Fabricated Using Four Different Additive Manufacturing Processes. *Metals* **2019**, *9*, 60. [CrossRef]

31. Gupta, S.K.; Shahidsha, N.; Bahl, S.; Kedaria, D.; Singamneni, S.; Prasad, K.D.V.Y.; Suwas, S.; Chatterjee, K. Enhanced biomechanical performance of additively manufactured Ti-6Al-4V bone plates. *J. Mech. Behav. Biomed. Mater.* **2021**, *119*, 104552. [CrossRef]

32. Shi, W.T.; Wang, P.; Liu, Y.D.; Hou, Y.J.; Han, G.L. Properties of 316 L formed by a 400 W power laser Selective Laser Melting with 250 μm layer thickness. *Powder Technol.* **2020**, *360*, 151–164. [CrossRef]

33. Miao, X.; Liu, X.; Lu, P.; Han, J.; Duan, W.; Wu, M. Influence of Scanning Strategy on the Performances of GO-Reinforced Ti6Al4V Nanocomposites Manufactured by SLM. *Metals* **2020**, *10*, 1379. [CrossRef]

34. Huang, W.; Chen, X.; Huang, X.; Wang, H.; Zhu, Y. Anisotropic Study of Ti6Al4V Alloy Formed by Selective Laser Melting. *JOM* **2021**, *73*, 3804–3811. [CrossRef]

35. Wang, J.; Wu, W.J.; Jing, W.; Tan, X.; Bi, G.J.; Tor, S.B.; Leong, K.F.; Chua, C.K.; Liu, E. Improvement of densification and microstructure of ASTM A131 EH36 steel samples additively manufactured via selective laser melting with varying laser scanning speed and hatch spacing. *Mater. Sci. Eng. A* **2019**, *746*, 300–313. [CrossRef]

36. Jamison, L.; Bartlett, L.X.D. An overview of residual stresses in metal powder bed fusion. *Addit. Manuf.* **2019**, *27*, 131–149.

37. Zou, S.; Xiao, X.Y.; Li, Z.C.; Liu, M.; Zhu, C.; Zhu, Z.; Chen, C.T.; Zhu, F. Comprehensive investigation of residual stress in selective laser melting based on cohesive zone model. *Mater. Today Commun.* **2022**, *31*, 103283. [CrossRef]

38. Ko, K.-H.; Kang, H.-G.; Huh, Y.-H.; Park, C.-J.; Cho, L.-R. Effects of heat treatment on the microstructure, residual stress, and mechanical properties of Co–Cr alloy fabricated by selective laser melting. *J. Mech. Behav. Biomed. Mater.* **2022**, *126*, 105051. [CrossRef]

39. Liu, Y.; Yang, Y.Q.; Wan, D. Investigation into the shrinkage in Z-direction of components manufactured by selective laser melting (SLM). *Int. J. Adv. Manuf. Technol.* **2017**, *90*, 2913–2923. [CrossRef]

40. Yan, T.-Q.; Chen, B.-Q.; Ji, X.; Guo, S.-Q. Influence of hot isostatic pressing on microstructure, properties and deformability of selective laser melting TC4 alloy. *China Foundry* **2021**, *18*, 389–396. [CrossRef]

41. Sun, Q.-D.; Sun, J.; Guo, K.; Waqar, S.; Liu, J.-W.; Wang, L.-S. Influences of processing parameters and heat treatment on microstructure and mechanical behavior of Ti-6Al-4V fabricated using selective laser melting. *Adv. Manuf.* **2022**, *73*, 3804–3811. [CrossRef]

42. Wang, Q.; Kong, J.; Liu, X.; Song, X.; Dong, K.; Yang, Y. Effect of Overlapping Remelting on Microstructures and Mechanical Properties of Selective Laser-Melted Ti-6Al-4V Alloy. *Adv. Eng. Mater.* **2022**, *24*, 2100876. [CrossRef]

43. Wei, W.-H.; Shen, J. Effect of laser energy density on microstructures and mechanical properties of selective laser melted Ti-6Al-4V alloy. *Int. J. Mater. Res.* **2018**, *109*, 437–442. [CrossRef]

44. Dzugan, J.; Seifi, M.; Prochazka, R.; Rund, M.; Podany, P.; Konopik, P.; Lewandowski, J. Effects of thickness and orientation on the small scale fracture behaviour of additively manufactured Ti-6Al-4V. *Mater. Charact.* **2018**, *143*, 94–109. [CrossRef]

45. Thijs, L.; Verhaeghe, F.; Craeghs, T.; Van Humbeeck, J.; Kruth, J.P. A study of the microstructural evolution during selective laser melting of Ti–6Al–4V. *Acta Mater.* **2010**, *58*, 3303. [CrossRef]